Resolving the Martensitic Transformation in Q&P Steels *In-Situ* at Dynamic Strain Rates Using Synchrotron X-ray Diffraction

CHRISTOPHER B. FINFROCK, BENJAMIN ELLYSON, C. GUS BECKER, JOHN COPLEY, KAMEL FEZZAA, NIRANJAN PARAB, TAO SUN, CODY KIRK, NESREDIN KEDIR, WEINONG CHEN, AMY CLARKE, and KESTER CLARKE

The dynamic deformation response of two quenching and partitioning (Q&P) steels was investigated using a high strain rate tension pressure bar and *in-situ* synchrotron radiography and diffraction. This allowed for concurrent measurements of the martensitic transformation, the elastic strains/stresses on the martensite and ferrite, and the bulk mechanical behavior. The steel with the greater fraction of ferrite exhibited greater ductility and lower strength, suggesting that dislocation slip in ferrite enhanced the deformability. Meanwhile, the kinetics of the martensitic transformation appeared similar for both steels, although the steel with a greater ferrite fraction retained more austenite in the neck after fracture.

https://doi.org/10.1007/s11661-022-06788-x

THE transformation-induced plasticity (TRIP) effect is increasingly being used to enhance the mechanical properties of engineered materials.[1] The TRIP effect is observed when a metastable phase undergoes a deformation-induced martensitic transformation (DIMT), and a combination of martensite variant selection[2] and dislocation generation[3] causes strain accommodation and hardening. The TRIP effect is of particular interest for high-toughness materials designed for high strain rate deformation. For instance, the TRIP effect is being explored for steels used in vehicle crash structures[4] and in blast or penetration-resistant armor.[5]

Quenching and partitioning (Q&P) steels,[6–8] an emerging class of TRIP-assisted advanced high strength steels (AHSS), are of particular importance because of their affordability and high strength. Q&P steels are candidates for use in vehicle crash structures, so it is necessary to understand the kinetics of DIMT so that the TRIP effect can be tailored for enhanced crash performance. DIMT responds to increases in the strain rate by several mechanisms. First, shear band intersections, which act as potential nucleation sites for martensite, tend to increase in number at high strain rates.[9,10] Second, as strain rates increase, the heat produced during deformation has less time to disperse into the environment, and so the temperature of the steel rises.[11,12] Rising temperatures reduce the driving force for DIMT, and thus reduce the propensity for martensite to nucleate at a potential nucleation site.[13–15] In a previous work by the authors, it was shown that the mechanical properties of a commercially available "QP980" steel were sharply strain rate sensitive; increasing the strain rate from 10^{-4} to 10^{-1} s^{-1} decreased the strain hardening rate, and thus the ductility.[16,17] In a subsequent investigation, it was shown that adiabatic heating and strain rate variations exhibited dissonant effects on the DIMT kinetics in QP980; that is, increasing the strain rate appeared to enhance the martensitic transformation, while adiabatic heating appeared to suppress the martensitic transformation.[18] A limitation of the previous studies was that the maximum strain rate tested was 10^{-1} s^{-1}; meanwhile, vehicle crashes impart deformation at much higher strain rates, up to approximately 10^3 s^{-1}.[19,20] Thus, it is also prudent to study mechanical properties and DIMT at dynamic rates.

CHRISTOPHER B. FINFROCK, BENJAMIN ELLYSON, C. GUS BECKER, AMY CLARKE and KESTER CLARKE are with the Department of Metallurgical and Materials Engineering, Colorado School of Mines, 1500 Illinois Street, Golden, CO 80401. Contact e-mail: christopher.b.finfrock@gmail.com JOHN COPLEY is with the Department of Geosciences, Princeton University, Guyot Hall, Princeton, NJ 08544. KAMEL FEZZAA, and NIRANJAN PARAB are with the Argonne National Laboratory, 9700 S. Cass Avenue, Lemont, IL 60439. TAO SUN is with the Department of Materials Science & Engineering, University of Virginia, 395 McCormick Road, Charlottesville, VA 22904. CODY KIRK, NESREDIN KEDIR, and WEINONG CHEN are with the Schools of Aeronautics/Astronautics and Materials Engineering, Purdue University, 701 West Stadium Avenue, West Lafayette, IN 47907.

Manuscript submitted March 28, 2022; accepted July 21, 2022.

Some details about microstructure evolution and DIMT kinetics in AHSS have been resolved using interrupted high-rate tests; for instance, Yang *et al.* showed that the progression of DIMT was more pronounced at 10^3 than at $10^{-3}\ s^{-1}$.[21] However, with interrupted tests, it is difficult to measure microstructure and phase fraction evolution with sufficient strain resolution, which obstructs fitting the measured DIMT data to empirical kinetics models.[22] Furthermore, the strain path dependence of DIMT could bias the data; for instance, Du *et al.* showed that strain incompatibility between the phases in a Q&P steel can cause reverse plastic strains upon unloading of interrupted test specimens,[23] which could cause further DIMT during unloading. The *ex-situ* X-ray diffraction technique also lacks the ability to measure stresses/strains on individual phases, which is problematic because this information could be useful to further tailor the DIMT behavior.

To inform better microstructure designs for metastable alloys, experimental configurations are needed that concurrently resolve the bulk mechanical properties, the constituent phase volume fractions, and the stresses on each phase. For quasi-static tests, these tools have become increasingly available at synchrotron and neutron radiation facilities. However, until recently, the scientific community has lacked the capability to perform such experiments at high strain rates. Here, we use a state-of-the-art synchrotron-based tool[24–26] developed at the 32-ID beamline at the Advanced Photon Source (APS) at Argonne National Laboratory (ANL), to collect radiography and diffraction videos of Q&P steels deformed at dynamic strain rates using a high-rate pressure bar. For the first time, high-speed radiography and high-energy X-ray diffraction (HEXRD) videos were collected *in-situ*, while the Q&P steels were deformed at $10^3\ s^{-1}$, to elucidate the link between DIMT kinetics and mechanical performance at dynamic rates.

Two commercially produced, Zn-coated C-Mn-Si steels were selected for this study. The steels were intercritically annealed to form approximately 25 and 15 volume percent intercritical ferrite. Subsequently, the steels were subjected to a Q&P process, leading to UTS values of 980 and 1180 MPa, respectively, for the microstructures containing higher and lower fractions of ferrite. Here, steels are designated based on strength level; for example, "QP980" refers to a steel with a UTS of 980 MPa. The chemical composition and thickness of each steel is listed in Table I. In a previous paper, QP980 and QP1180 were characterized by a combination of optical microscopy, scanning electron microscopy (SEM), lab-scale X-ray diffraction (XRD), and tensile testing at quasi-static rates.[8] With XRD, it was determined that each steel contained approximately 12 volume percent austenite, with intercritical ferrite and martensite occupying the remainder of the microstructure. The austenite existed in both blocky and film-type morphologies. The martensitic fraction of the microstructure appeared to be slightly tempered from the carbon partitioning step of the Q&P thermal cycle.[8] Tensile specimens, with a gauge length of 4 mm and a width of 1 mm, were machined parallel to the rolling direction of QP980 and QP1180 using wire electrical discharge machining. Subsequently, they were metallographically ground and polished to a final thickness of approximately 200 μm, to minimize the X-ray absorption by the samples. It is noted that the comparatively small dimensions of the tensile specimens may have influenced the mechanical responses and kinetics of DIMT that are presented hereafter. For instance, the strain state or constraint of the specimens could be different relative to conventional bulk specimens, which could influence the kinetics of DIMT. Furthermore, surface damage due to machining could increasingly dictate the perceived properties of small tensile specimens, because the damaged volume is large relative to the total sample volume.[27]

The Sector 32-ID beamline at the APS is equipped with several high-rate tension and compression pressure bars, along with imaging equipment capable of resolving fracture and phase evolution with sub-microsecond temporal resolution. Details of the beamline configuration are documented by Hudspeth *et al.*[24,25] A polychromatic undulator pink beam was used due to its relatively high intensity and pulse frequency. The beam had a nominal first harmonic energy of 24.65 keV (created with a 13 mm undulator gap) and was adjusted using slits to a width of 2 mm and a height of 1 mm. Radiography videos were recorded using a Photron FASTCAM SA-Z equipped with a LuAG:Ce scintillator at ≈50,000 frames per second. Simultaneously, diffracted rings were recorded in the transmission mode with a Shimadzu HPV-X2 equipped with a LSO:Ce scintillator at ≈200,000 frames per second. A modified tension bar equipped with a fast-response load cell was used for the experiments.[26] A schematic of the tension bar, the radiography and diffraction cameras, and the synchrotron beam are shown in Figure 1(a).

Four replicate samples for each test condition were deformed at a strain rate of approximately $10^3\ s^{-1}$. To exemplify the *in-situ* data that were collected during the experiments, representative radiography and diffraction frames at various stages of deformation are shown in Figure 1(b and c). In Figure 1(b), radiography images for QP1180 are shown during uniform elongation, necking, and fracture. For each specimen, diffuse necking occurred first, followed by localized thinning at the final location of fracture. In Figure 1(c), a diffraction image for the same specimen prior to deformation is shown; HiSPoD, a MATLAB-based diffraction analysis toolbox developed at the 32-ID beamline,[28] was implemented to radially integrate the diffraction image, leading to the one-dimensional "lineout" shown in Figure 1(c). The theoretical locations of the BCC(002), BCC(112), BCC(022), FCC(022), FCC(113), and FCC(222) peaks are labelled in the diffraction image and the lineout.

Engineering stress-strain curves for QP980 and QP1180, deformed at $10^3\ s^{-1}$, are shown in Figure 2(a). Undulations in the stress-strain curves of both steels were evident; these undulations may have been due to the dynamic nature of the experiment,

Table I. Composition and Phase Fraction of Each Q&P Steel

Steel	C (Wt Pct)	Mn (Wt Pct)	Si (Wt Pct)	Austenite* (Vol Pct)	Ferrite** (Vol Pct)	Martensite (Vol Pct)
QP980	0.201	1.93	1.62	11.3	≈25	balance
QP1180	0.204	2.26	1.74	11.4	≈15	balance

*Austenite content was measured with lab-scale X-ray diffraction.
**Ferrite content was measured with optical microscopy.

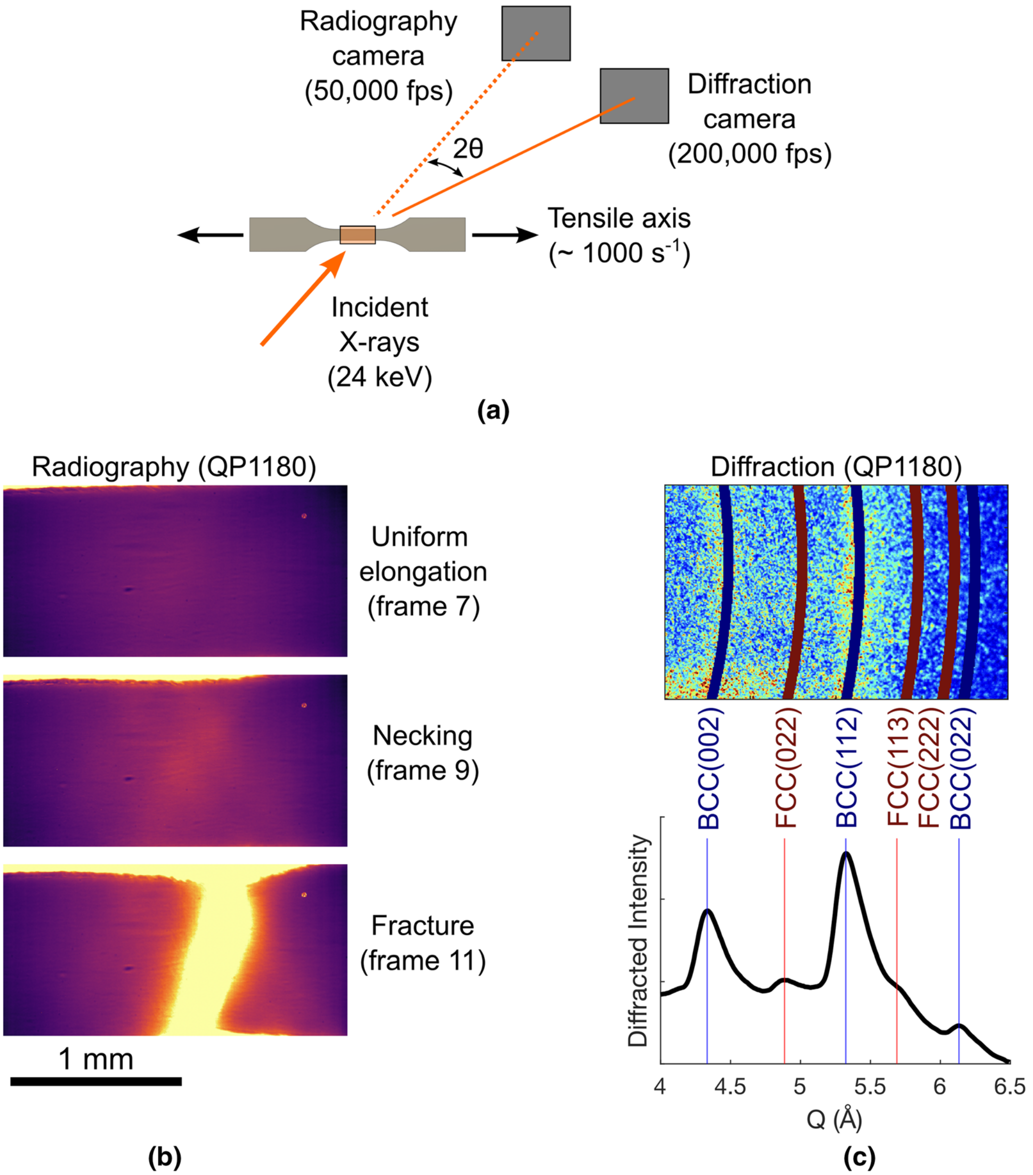

Fig. 1—(*a*) Configuration of the tensile specimen relative to the X-ray beam axis, radiography camera, and diffraction camera. The cross-section of the X-ray beam (1 mm × 2 mm) is shown schematically with the orange rectangle in the center of the tensile specimen. (*b*) Representative radiography images recorded during uniform elongation, necking, and fracture of a QP1180 specimen using an acquisition rate of 50,000 images per second. (*c*) Representative diffraction data of the same specimen *prior to deformation*, collected using an acquisition rate of 200,000 images per second. The predicted locations of various peaks are superimposed on the image. Each diffraction image was radially integrated using HiSPoD software; an example lineout for QP1180 prior to deformation is shown (Color figure online).

where the deformation was not homogeneous due to stress wave propagation along the length of the sample. More specifically, the undulations are thought to be caused by elastic compliance in the vicinity of the load cell.[29] The QP980 generally exhibited a higher elongation and a lower yield stress, relative to QP1180.

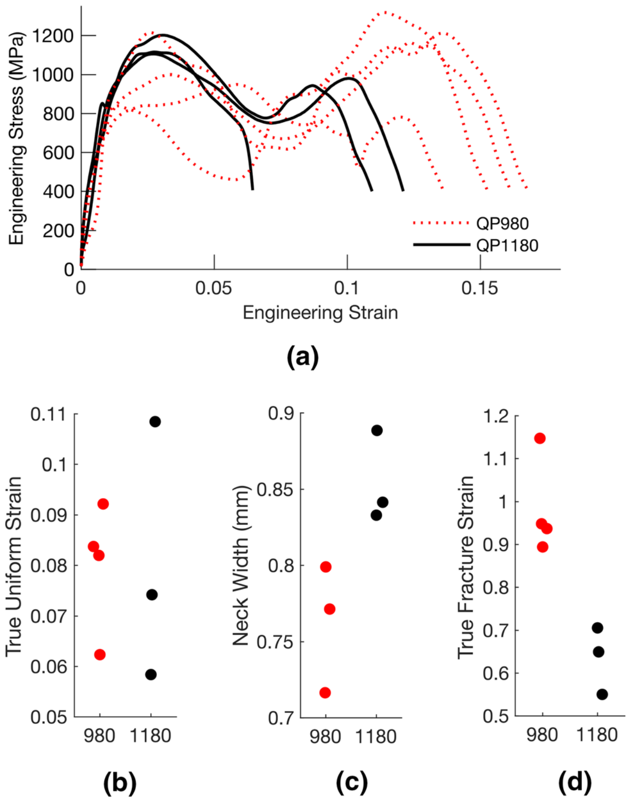

Fig. 2—(*a*) Stress-strain curves for both steels deformed at an engineering strain rate of approximately $10^3\ s^{-1}$. Measures of bulk ductility for both steels: (*b*) true uniform strain, (*c*) neck width, and (*d*) true fracture strain.

Interestingly, the measured stresses were similar to those observed previously at strain rates of 10^{-4} to $10^{-1}\ s^{-1}$; this suggests that a strain rate dependence of the flow stress was not obvious.[16]

Based on the stress-strain curves, it was apparent that the total elongation was large relative to the uniform elongation, especially for QP1180. This suggested that most of the strain was localized in the neck. Meanwhile, the radiography videos showed that diffuse and localized necking occurred for both steels. To quantitatively access the bulk ductility, several measurements of the fractured specimens were collected. True uniform strain was measured based on the cross-section of the sample, prior to deformation and after fracture in the uniformly elongated region of the gauge section. True fracture strain was calculated based on the area of the fracture surface after Dieter.[30] Neck width was measured using the radiography stills after fracture. Each steel exhibited relatively little uniform elongation (Figure 2(b)). Meanwhile, trends in the neck width (Figure 2(c)) and true fracture strain (Figure 2(d)) suggested that QP980 had a higher necking strain relative to QP1180. This confirmed that the structure-property relationships that exist in the steels at quasi-static strain rates also prevail at high rates. That is, the larger amount of ferrite in QP980 enhanced the ductility at both quasi-static and dynamic rates.

To measure the evolution of austenite content as a function of deformation time, HiSPoD was used to create HEXRD lineouts at time increments of five microseconds. Despite the use of synchrotron light, which is on the order of one quadrillion-times brighter than a common lab diffractometer, the minuscule exposure times used in this experiment greatly limited the HEXRD signal that was collected by the detector. Three steps were taken to improve the signal-to-noise ratio of the lineouts. First, the diffracted intensities detected by each pixel were smoothed by pixels existing in adjacent Q-space. Second, the lineouts were also smoothed over adjacent time increments. Finally, the lineouts for each of the four replicates from each steel were summed. After this processing, the integrated intensities of the three lowest-index peaks captured in the experiment, BCC(002), FCC(022), and BCC(112), were plotted over time in Figure 3(a). Meanwhile, the FCC(113), FCC(222), and BCC(022) peaks were omitted because their height was barely above the background; the low signal of those peaks was likely due to their comparatively low structure factor. The average onset of straining and fracture are annotated with a black horizontal line, while the peak position prior to straining is plotted with a red vertical line.

Changes in the intensity of the peaks were observed over time, which suggested that the number of grains that met a diffraction condition changed during deformation. For instance, the BCC(002) peak appeared to slightly diminish in intensity for both steels, which could be due to small changes in crystallographic texture during plastic deformation, thus rotating crystals out of a diffraction condition. The FCC(022) appeared to strongly diminish in intensity for both steels. DIMT was likely responsible for this shift; DIMT could have facilitated a reduction in the total volume fraction of austenite, and thus a decrease in the diffracted intensity of FCC(022) over time. Finally, the BCC(112) appeared to exhibit relatively consistent intensity throughout the deformation process.

Deviations from the peak position (Q) prior to straining were observed for each steel and diffraction peak. These peak shifts were due to the elastic lattice strains associated with mechanical loading of the tensile specimens. After the d-spacing of each family of planes (d^{hkl}_{ε}) was determined with Bragg's law, the elastic lattice strains (e^{hkl}_{ε}) were calculated using Eq. [1]:

$$e^{hkl}_{BCC} = \frac{d^{hkl}_{\varepsilon} - d^{hkl}_{\varepsilon=0}}{d^{hkl}_{\varepsilon=0}} \qquad [1]$$

The evolution of e^{002}_{BCC} and e^{112}_{BCC} are plotted in Figure 3(b,c), respectively. There was no obvious difference in the lattice strains between QP980 and QP1180, which suggested that any difference was less than the practical spatial resolution of the diffraction setup. A similar analysis was performed for the FCC(022) reflection, but the signal-to-noise ratio of that peak, along with the decreasing peak height due to DIMT, made the analysis unreliable. The stresses nominally parallel to the tensile axis for the BCC(112)

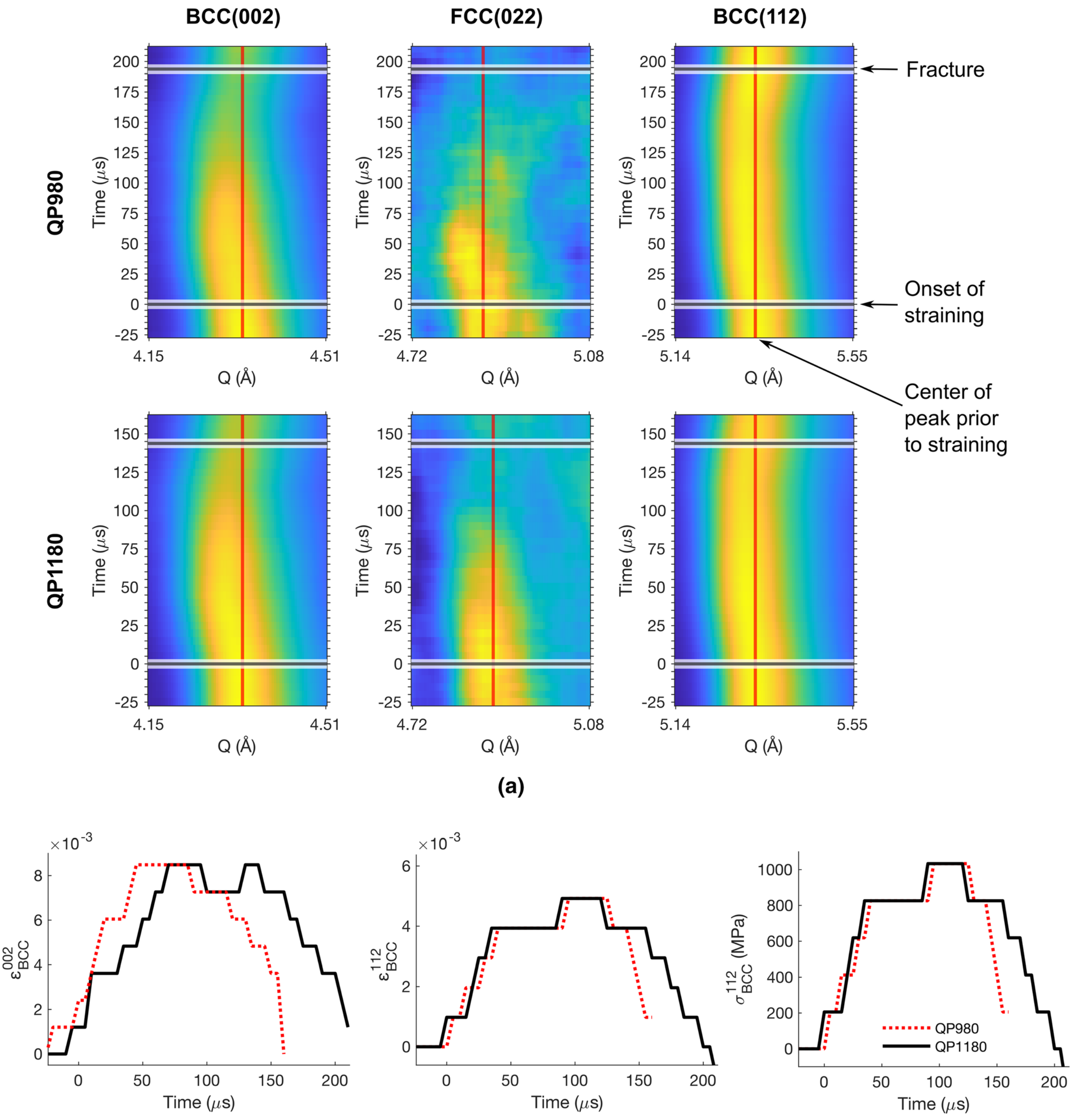

(a)

(b)

(c)

(d)

Fig. 3—(*a*) Intensity change over time measured *in-situ* for the BCC(002), FCC(022), and BCC(112) peaks. (*b*, *c*) Elastic strains on the BCC(002) and BCC(112) peaks, respectively. (*d*) Stress on the BCC(112) peak, calculated based on Hooke's law and an assumed elastic modulus (E^{112}_{BCC}) of 210 GPa.[31] The steps in each curve (b-d) are indicative of the minimum spatial resolution of the diffractometer, which was controlled by the pixel density of the diffraction camera.

peak, σ^{112}_{BCC}, were estimated based upon Hooke's law using Eq. [2][31]:

$$\sigma^{112}_{BCC} = E^{112}_{BCC} e^{112}_{BCC} \qquad [2]$$

where E^{112}_{BCC} was assumed to be equal to 210 GPa after Harjo *et al.*[31] σ^{112}_{BCC} appeared to be relatively similar for each steel; the maximum σ^{112}_{BCC} was equal to 1030 ± 100 MPa for both steels. Interestingly, the stresses measured by diffraction appeared to be less sensitive to ringing artifacts than the stresses measured by the tension bar. Perhaps this was because the bulk measurement of stress *via* HEXRD was insensitive to the non-homogeneous strain wave propagation; that is, strain wave propagation is a spatially and temporally

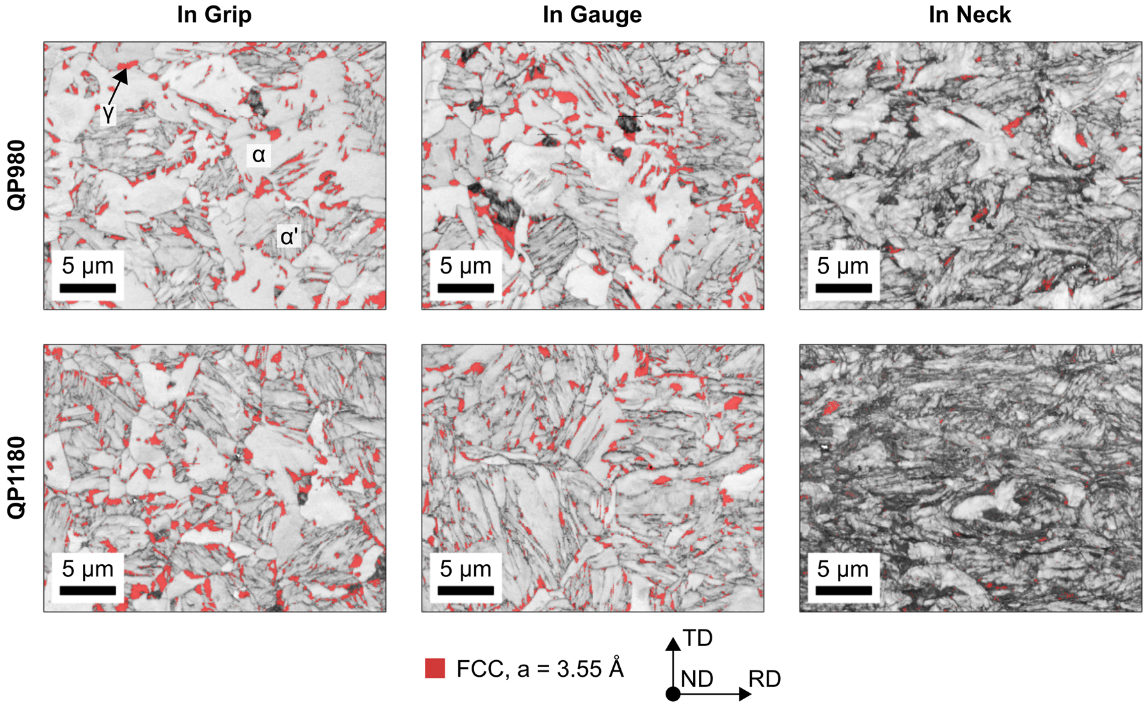

Fig. 4—EBSD image quality + austenite (FCC) phase maps for each steel, with progressively increasing applied tensile strain. From left to right: in the grip (zero strain), the uniformly elongated gauge section, and the necked region.

localized phenomenon that is difficult to detect with volume-averaged bulk techniques.

After the beamtime, electron backscatter diffraction (EBSD) maps in the normal direction plane were collected in the grip, gauge, and neck. The EBSD maps were used to evaluate the microstructure development, and to confirm that DIMT was the root cause of the diminished intensity of the FCC(022) reflection. Figure 4 shows EBSD image quality (IQ) + austenite (FCC) phase maps overlaid for each steel. In the grip, the starting microstructure of each steel is evident. Three phases were present: ferrite, which formed during the intercritical annealing process and indexed as BCC with a relatively high IQ and minimal substructure; martensite, which indexed as BCC and exhibited a substantial lath substructure; and austenite, which indexed as FCC and existed in small blocky and film shapes. Prior to deformation, both microstructures looked similar, with the key difference being that the QP1180 appeared to contain less ferrite and more martensite.

In the uniformly elongated section of the gauge, the IQ slightly decreased, which was especially noticeable in the ferrite. Although not shown here, this decrease in the IQ was accompanied by an increase in the lattice rotation in large ferrite grains, which was manifest by larger orientation deviation from grain center to edge. Relative to the scans in the grip section and in the uniformly elongated gauge section, the scans collected in the neck of both steels exhibited a strong refinement of the substructure in every phase, along with a large deterioration in IQ. The austenite content changed in a similar manner; no strong change in austenite content was observed between the scans in the grip and in the uniformly elongated gauge section, but the austenite content in the neck of both steels decreased extensively. Together, the observations of strong evolution of IQ and austenite content during necking suggested that both the TRIP effect and dislocation slip accommodated the necking strains, despite the high effective strains and temperature rises associated with neck formation at dynamic strain rates.

With a true fracture strain of approximately one, EBSD analysis showed that several volume percent austenite remained untransformed within the neck in QP980, which suggested that the surviving austenite was exceedingly stable during high-rate deformation. Meanwhile, the DIMT behavior of QP1180 diverged, where a smaller fraction of austenite existed after necking, despite a lower true fracture strain of approximately 0.6. This suggested that the austenite in QP1180 was less stable under similar deformation conditions. This could have been caused by the higher ratio of martensite to ferrite in QP1180, which could have promoted stress partitioning (that is, disproportionate mechanical loading) to the austenite. This insight gained by EBSD analysis was not supported by the *in-situ* bulk diffraction data. Because the bulk diffraction analysis was qualitative in nature due to the low signal-to-noise ratio, it was impossible to compare the measured austenite fractions existing with phase amounts less than several volume percent. A greater signal-to-noise ratio would be required to quantify the DIMT kinetics in heavily deformed microstructures containing only a few percent austenite. In the future, a greater signal-to-noise ratio may be achieved with the development of higher sensitivity high-rate cameras and higher brightness beamline configurations.

The maturation of bulk diffraction tools with excellent temporal resolution has provided new opportunities to understand the deformation of materials at high strain rates. Here, the dynamic tensile mechanical properties of QP980 and QP1180 were measured, while DIMT was characterized with a combination of *in-situ* diffraction imaging and *ex-situ* EBSD. The QP980, which contained a higher fraction of soft ferrite, exhibited a lower yield strength and a higher ductility. During deformation, the strains and stresses on the BCC-indexed phases were tracked, and they appeared to be similar between the two steels, to within the practical spatial resolution of the diffraction detector. Meanwhile, the austenite content in both steels appeared to decrease similarly, prior to the formation of a neck. After a neck formed, EBSD showed that the austenite in QP980 appeared to exhibit a slightly greater stability as a function of true strain. Continued experiments in this field, coupled with enhancements in resolution and signal-to-noise ratio in bulk diffraction experiments, will elucidate the fundamental relationships between microstructure development and mechanical performance during deformation at dynamic strain rates.

ACKNOWLEDGMENTS

Christopher Finfrock acknowledges the financial support of the Advanced Steel Processing and Products Research Center (ASPPRC), an industry-university cooperative research center at the Colorado School of Mines, Golden, CO. Benjamin Ellyson, C. Gus Becker, and John Copley acknowledge the support of the Center for Advanced Non-Ferrous Structural Alloys (CANFSA), a National Science Foundation (NSF) IUCRC (Award No. 1624836) at the Colorado School of Mines, Golden, CO. Christopher Finfrock and Kester Clarke acknowledge support from the National Science Foundation division of Civil, Mechanical and Manufacturing Innovation (NSF-CMMI) through award no. 1752530. This research used resources of the Advanced Photon Source, a U.S. Department of Energy (DOE) Office of Science User Facility operated for the DOE Office of Science by Argonne National Laboratory under Contract No. DE-AC02-06CH11357.

CONFLICT OF INTEREST

On behalf of all authors, the corresponding author states that there is no conflict of interest.

REFERENCES

1. W. Bleck, X. Guo, and Y. Ma: *Steel Res. Int*., 2017, vol. 88, p. 10. https://doi.org/10.1002/srin.201700218.
2. C.L. Magee: Transformation Kinetics, Microplasticity and Ageing of Martensite in Fe-31-Ni. PhD thesis, Carnegie Institute of Technologie University, Ph.D. Thesis (1966).
3. G.W. Greenwood, R.H. Johnson: *Proc. R. Soc. A*, 1965, vol. 283, 403–22. https://doi.org/10.1098/rspa.1965.0029.
4. D.K. Matlock, J.G. Speer, E. De Moor, P.J. Gibbs, *Jestech*, 2012, vol. 15, 1–12.
5. N.J. Wengrenovich, G.B. Olson: *Mater. Today*, 2015, vol. 2, pp. 639–42. https://doi.org/10.1016/j.matpr.2015.07.365.
6. J. Speer, D.K. Matlock, B.C. De Cooman, J.G. Schroth: *Acta Mater*., 2003, vol. 51, pp. 2611–22. https://doi.org/10.1016/S1359-6454(03)00059-4.
7. A.J. Clarke, J.G. Speer, M.K. Miller, R.E. Hackenberg, D.V. Edmonds, D.K. Matlock, F.C. Rizzo, K.D. Clarke, E. De Moor: *Acta Mater*., 2008, vol. 56, pp. 16–22. https://doi.org/10.1016/j.actamat.2007.08.051.
8. C.B. Finfrock, A.J. Clarke, G.A. Thomas, K.D. Clarke: *Metall. Mater. Trans. A*, 2020, vol. 51A, pp. 2025–34. https://doi.org/10.1007/s11661-020-05666-8.
9. S.S. Hecker, M.G. Stout, K.P. Staudhammer, J.L. Smith: *Metall. Trans. A*, 1982, vol. 13A, pp. 619–26. https://doi.org/10.1007/BF02644428.
10. L.E. Murr, K.P. Staudhammer, S.S. Hecker: *Metall. Trans. A*, 1982, vol. 13, pp. 627–35. https://doi.org/10.1007/BF02644428.
11. G.I. Taylor, H. Quinney, *Proc. R. Soc. Lond. Ser. A* , 1934, vol. 143, pp. 307–26. https://doi.org/10.1098/rspa.1934.0004.
12. Finfrock, C., Becker, C.G., Ballard, T., Thomas, G., Clarke, K., Clarke, A.: in Contributed Papers from Materials Science & Technology (MS &T19), Portland, Oregon, pp. 1236–43 (2019). https://doi.org/10.7449/2019/MST_2019_123.
13. J. Coryell, V. Savic, L. Hector, S. Mishra: Temperature Effects on the Deformation and Fracture of a Quenched-and-Partitioned Steel. SAE Technical Papers Technical Report No. 2013-01-0610 (2013). https://doi.org/10.4271/2013-01-0610.
14. W.A. Poling, E. De Moor, J.G. Speer, K.O. Findley: *Metals*, 2021, vol. 11, p. 2. https://doi.org/10.3390/met11020375.
15. C.B. Finfrock, B. Ellyson, S.R.J. Likith, D. Smith, C.J. Rietema, A.I. Sav-Ille, M.M. Thrun, G. Becker, A.L. Araujo, E.J. Pavlina, J. Hu, J.-S. Park, A.J. Clarke, K.D. Clarke: *Acta Mater*., 2022. https://doi.org/10.1016/j.actamat.2022.118126.
16. C.B. Finfrock, M.M. Thrun, D. Bhattacharya, T. Ballard, A.J. Clarke, K.D. Clarke, *Metall. Mater. Trans. A* , 2021, vol. 52A, pp. 928–42. https://doi.org/10.1007/s11661-020-06127-y.
17. C.B. Finfrock: Temperature and Strain Rate Dependence of the Martensitic Transformation and Mechanical Properties in Advanced High Strength Steels. PhD thesis, Colorado School of Mines, Golden, CO (May 2022).
18. C.B. Finfrock, D. Bhattacharya, B.N.L. McBride, T.J. Ballard, A.J. Clarke, K.D. Clarke: *JOM*, 2022, vol. 74, pp. 506–12. https://doi.org/10.1007/s11837-021-05039-5.
19. R. Alturk, L.G. Hector, C. Matthew Enloe, F. Abu-Farha, T.W. Brown: *JOM*, 2018, vol. 70, pp. 894–905. https://doi.org/10.1007/s11837-018-2830-3.
20. C. Enloe, V. Savic, W. Poling, L. Hector, R. Alturk: Strain Rate Effect on Martensitic Transformation in a TRIP Steel Containing Carbide-Free Bainite. SAE Technical Papers, Technical Report No. 2019-01-0521, 1–10 (2019). https://doi.org/10.4271/2019-01-0521.
21. X. Yang, X. Xiong, Z. Yin, H. Wang, J. Wang, D. Chen: *Exp. Mech*., 2014, vol. 54, pp. 641–52. https://doi.org/10.1007/s11340-013-9828-0.
22. G.B. Olson, M. Cohen: *Metall. Trans. A*, 1975, vol. 6A, pp. 791–95. https://doi.org/10.1007/BF02672301.
23. H. Du, Y. Gong, T. Liang, Y. Li, Y. Xu, X. Lu, Q. Zeng, X. Jin: *Metall. Mater. Trans. A*, 2020, vol. dA, pp. 2097–2117. https://doi.org/10.1007/s11661-020-05701-8.
24. Hudspeth, M., Claus, B., Dubelman, S., Black, J., Mondal, A., Parab, N., Funnell, C., Hai, F., Qi, M.L., Fezzaa, K., Luo, S.N., Chen, W.: *Rev. Sci. Instrum*., 2013, vol. 84, p. 2. https://doi.org/10.1063/1.4789780.
25. M. Hudspeth, T. Sun, N. Parab, Z. Guo, K. Fezzaa, S. Luo, W. Chen: *J. Synchr. Radiat*., 2015, vol. 22, pp. 49–58. https://doi.org/10.1107/S1600577514022747.
26. C.D. Kirk, N.D. Parab, N. Kedir, Z. Guo, Y. Nie, S. Paulson, J. Thomas, K. Fezzaa, T. Sun, W. Chen: *Exp. Mech*., 2019, vol. 59, pp. 805–18. https://doi.org/10.1007/s11340-019-00524-0.

27. K. Kumar, A. Pooleery, K. Madhusoodanan, R.N. Singh, J.K. Chakravartty, B.K. Dutta, R.K. Sinha:*Proc. Eng.*, 2014, 86, pp. 899–909. https://doi.org/10.1016/j.proeng.2014.11.112.
28. T. Sun, K. Fezzaa: *J. Synchr. Radiat.*, 2016, vol. 23, pp. 1046–53. https://doi.org/10.1107/S1600577516005804.
29. M.A. Meyers: *Dynamic Behavior of Materials* (Wiley, New York, 1994).
30. G.E. Dieter: *Mech. Metall.*, 3rd edn. (McGraw-Hill, New York, 1961).
31. S. Harjo, N. Tsuchida, J. Abe, W. Gong: *Sci. Rep.*, 2017, vol. 7, pp. 2–4. https://doi.org/10.1038/s41598-017-15252-5.